

## Chapter X

### Structure of sheared cohesive granular bulk

**Lothar Brendel, Alexander Weuster, and Dietrich E. Wolf;  
Harald Zetzener, Stephan Strege, Lutz Torbahn, and Arno Kwade;  
Lisa Handl, and Volker Schmidt**

**Abstract** The particle-particle interactions on micro scale determine the macroscopic flow behaviour of bulk solids as in shear testers and in industrial facilities. However, although the flow behaviour can be measured on macro scale and bulk solid facilities as silos can be designed based on reliable engineering knowledge, the microscopic physics causing the wide fluctuation in flow properties of the different bulk solids is still not deeply understood. Therefore, the motion of individual particles in shear testers was determined experimentally as well as by discrete element method (DEM) simulations. The experimental detection of the particle motion was achieved by an own-built micro torsional shear tester which can be placed into a X-ray tomography device ( $\mu$ CT) and a customized statistical analysis method to extract the individual trajectories of almost all particles even at large angle increments of up to  $5^\circ$  between the single tomographic measurements. The two bulk solids, borosilicate glass beads and potassium chloride, with particle sizes in the range of 10 to 100  $\mu\text{m}$  show very different contact behaviour, on one side viscoelastic with constant adhesion force and on the other side elastoplastic with time dependent adhesion. By a careful calibration of the DEM contact model parameters using among others shear and nanoindentation tests the microscopic behaviour of the two different model materials could be simulated successfully to predict the shear bands and to determine the macroscopic flow properties. Moreover, a theory for the rate dependent rheology of granular materials showing time consolidation has been developed.

---

L. Brendel • A. Weuster • D. E. Wolf  
Faculty of Physics, Universität Duisburg-Essen, Duisburg, Germany  
e-mail: [dietrich.wolf@uni-due.de](mailto:dietrich.wolf@uni-due.de)

H. Zetzener • S. Strege • L. Torbahn • A. Kwade  
Institute Particle Technology, Technische Universität Braunschweig, Braunschweig, Germany  
e-mail: [a.kwade@tu-bs.de](mailto:a.kwade@tu-bs.de)

L. Handl • V. Schmidt  
Institute of Stochastics, Universität Ulm, Ulm, Germany  
e-mail: [volker.schmidt@uni-ulm.de](mailto:volker.schmidt@uni-ulm.de)

## 1. Introduction

Cohesive particle contacts have intrinsic kinetics, even if the particles do not move: Freshly formed contacts mature due to accommodation in the contact area of their rough surfaces, intensifying atomic binding and hence lowering the interfacial free energy. The underlying microscopic processes are very complex, because they can be influenced by various means, such as temperature, humidity, surface contaminants, or pressure. (Here we do not consider cementation in the sense that a foreign chemical substance forms a solid bridge between the particles, although the phenomenology should be similar.) All these parameters determine the characteristic time, on which the cohesion force between particles establishes itself. We call it *accommodation time*  $t_c$ .

The accommodation time can be probed in bulk powders by shearing: The idea is that shear localization, density inhomogeneities and anisotropic fabric reflect the microscopic competition between the accommodation time and the inverse shear rate. Hence a structural analysis of powder bulk sheared at different *rates*, will reveal properties of the contact mechanics. In this project review two model materials are considered, which represent opposite limiting cases. Glass spheres at room temperature have a very short accommodation time. Cohesion (due to van der Waals forces) is instantaneously present, when a contact forms, and does not increase noticeably, when it lasts (Section 4). On the other hand, KCl-particles are a clear example for caking contacts, where the cohesion force becomes slowly stronger (Section 2.3.3). A completely caked powder resembles a porous solid rather than a granular medium. Instead of a shear band one expects a crack, which upon continued shear grinds the adjacent material, so that it becomes granular-like. Section 3 explores this process theoretically.

In order to investigate the bulk structure evolution, a novel experimental tool has been developed, the micro shear tester, combined with x-ray tomography, which allows grain-resolved rheological observations. The experiments are briefly reviewed in Section 2.1. Statistical particle tracking tools have been developed to analyze these experiments (Section 2.2). For connecting these results to contact mechanics, simulations with the discrete element method (DEM, see Section 2.3) are indispensable. Such interdisciplinary efforts are needed to shed light on the question, what information about contact mechanics can be extracted from shear induced bulk structures.

## 2. Methods to study grain-resolved rheology

### 2.1 Micro shear tester and tomography, requirements for model materials

For the investigation of the particle motion and the subsequent change in powder structure a novel micro torsional shear tester was developed within the project. The shear tester was designed to be integrated into a high resolution XMT device (MicroXCT 400, Xradia, Inc., today Zeiss). This state of the art XMT scanner differs from the conventional scanners due to the implementation of special scintillators in combination with optical magnifying lenses (see e.g. [Str14a]). The micro shear tester has a cylindrical shear cell with inner diameters from less than 2 mm to about 4 mm and allows a precise compaction and shear deformation of the small

powder samples in the lower  $\mu\text{L}$ -range (typically around  $10\ \mu\text{L}$ ) [Str14a]. Another characteristic of this novel shear device is the decoupled and most precise determination of the acting forces and torque behavior whereas the whole system is theoretically frictionless using advanced technology of magnetic spring and air bearing mechanisms. Due to the implemented very precise position and force sensors the tester can be operated in strain or stress controlled mode. The possible axial deformations range from micrometres to several millimetres and the resulting normal and shear stresses from 0.5 to 30 kPa. By the combination of  $\mu\text{ST}$  and XMT, Fig. 1 (left), a stepwise manipulation of the specimen can be performed in order to acquire high resolution 3D images in between these deformation steps. During the whole measurement the specimen remains in the scanning position and thus, the danger of potentially disturbing the fragile structure is minimized.

The cylindrical shear cell with the powder sample is exposed to the x-ray beam. The X-ray source was operated with an acceleration voltage of 50 kV and a constant current intensity of  $200\ \mu\text{A}$ . The specific absorption of the specimen due to its material and inner structure results in a characteristic radiograph, which the scintillator translates into the spectrum of visible light. The subsequent optical lens generates the required magnification of the image. In order to change the magnification the optical lens can be replaced using an objective revolver. For the usually applied shear cell diameter of 2 mm, a ten-fold optical magnification was adequate to image the entire cell with a resolution of  $2.2\ \mu\text{m}$  (2x binning). The 3D information is achieved by multiple projections while the sample rotates in small angle steps around its vertical axis. A record of 2000 two-dimensional projections provides the basis for a precise three-dimensional reconstruction of the powder microstructure.

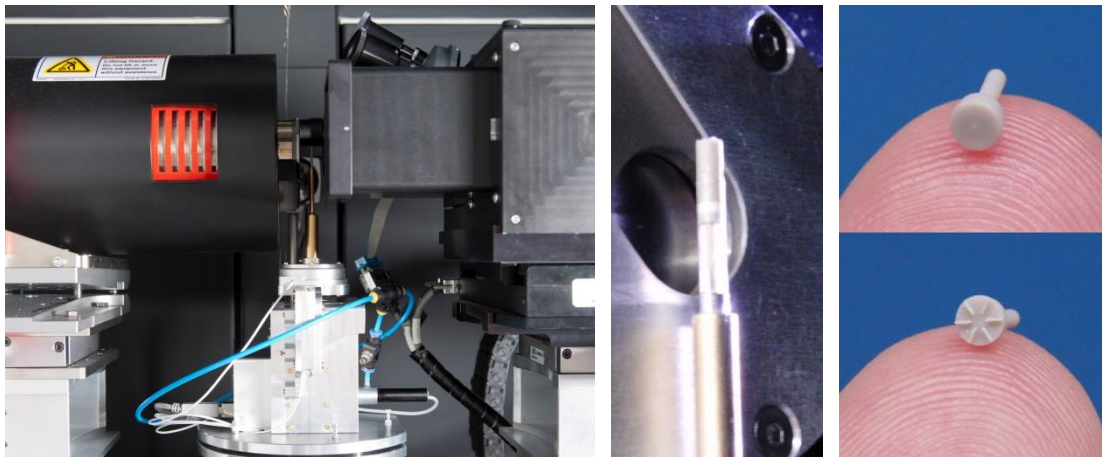


**Fig. 1:** Integration of the  $\mu\text{ST}$  into the XMT system (left), powder specimen in front of the x-ray source (centre), compression and shear geometry on a fingertip (right) [Str14a].

In order to minimize the x-ray absorption the shear cell was build out of materials with low effective atomic number. Moreover, the thermal expansion coefficient should be as low as possible to avoid a geometrical change of the shear cell due to heat expansion. Therefore, for compression and shear tests the powder specimen is enclosed in a thin-walled borosilicate glass tube (wall thickness  $\approx 50\ \mu\text{m}$ , length 40 mm) with an effective atomic number of 10.7 and a

thermal expansion coefficient of only  $3.3 \cdot 10^{-6}/\text{K}$ . The top and bottom sides of the powder sample are limited by the upper and lower pistons made out of PEEK (effective atomic number of about 6, thermal expansion coefficient of  $47 \cdot 10^{-6}/\text{K}$ , Fig. 1 (centre, right)). While compaction experiments are performed in between two flat pistons, shear deformation can be induced with structured pistons. During the test the upper piston, which is firmly connected to the glass tube, performs a relative movement (i.e. translation or rotation) to the lower piston. In order to prevent agglomeration during the preparation process, powder is sieved into the capillary. After the filling process, the sample is compressed to the desired normal load, usually 0.5 kPa. During shear deformation the sidewall and the upper piston rotates stepwise. Usually during the first  $9.5^\circ$  of shear deformation an angle increment of  $0.5^\circ$  is set. Afterwards, the angle increment is raised to usually  $5^\circ$  until the final shear deformation is achieved. In most experiments a total shear deformation of  $39.5^\circ$  was used. The shear deformation is performed in a quasi-static regime using an angle velocity  $\omega$  of  $0.1^\circ/\text{s}$ . Between the shear steps tomographic data is recorded.

For  $\mu\text{CT}$  measurements the model particles have to fulfill specific requirements. On one side the effective atomic number should be high enough, at least in the range of 10. On the other side the particles should not be smaller than  $10 \mu\text{m}$  in order to get good resolved pictures of the particles and, at the same time, a full image of the powder sample on particle level inside the 2 mm wide shear cell. As cohesive model material with very short accommodation times due to van der Waals forces massive borosilicate glass beads (BSGMS 27-32  $\mu\text{m}$ , Cospheric, USA) are applied. Against that as model material for caking contacts potassium chlorid (KCl) particles are used (K+S, Germany). As depicted in Fig. 2 the BSGMS micro beads are very spherical, whereas the KCl particles show a prismatic to irregular shape. Moreover, the BSGMS particles have a very narrow particle size distribution ( $x_{10} \approx 20 \mu\text{m}$ ,  $x_{50} \approx 30 \mu\text{m}$ ,  $x_{90} \approx 40 \mu\text{m}$ ), while the size distribution of the specifically milled KCl particles is relatively wide ( $x_{10} \approx 3 \mu\text{m}$ ,  $x_{50} \approx 20 \mu\text{m}$ ,  $x_{90} \approx 50 \mu\text{m}$ ) [Str14b]. The mechanical characteristics of the single particles were determined by nanoindentation (Triboindenter, Hysitron, Inc., USA). For BSGMS particles a Young modulus of  $14.8 \pm 7.2 \text{ GPa}$  was achieved by fitting the deformation curve with the model of Hertz. The non-spherical KCl particles cannot be described by the model of Hertz, so that a contact stiffness of  $9.8 \pm 3.4 \text{ kN/m}$  was determined [Str14b]. The flowabilities of the two model powders were characterized within a Schulze ring shear tester RST-XS: The  $ff_c$  values of the BSGMS powder were above 10 for principal stresses higher than 8 kPa, so that the BSGMS powder can be characterized as free flowing. Against that for the KCl powder the  $ff_c$  values are in the range between 1.5 at low principal stresses and 3 at high principal stresses, so that the KCl powder has a very cohesive to cohesive flow behavior according to the definition of Jenike.

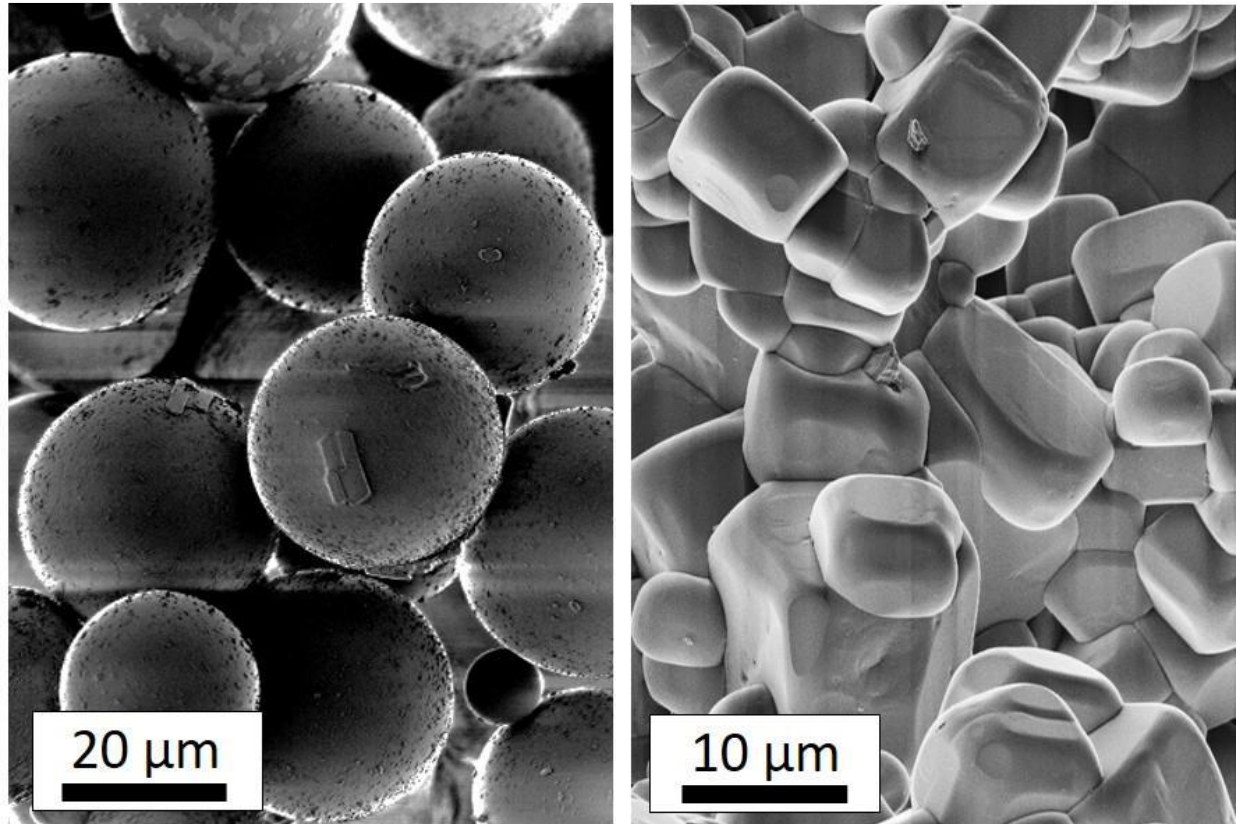


**Fig. 2** SEM images of model particles. Left: borosilicate glass micro spheres, Right: potassium chloride particles [Str14b]

## 2.2 Particle tracking and statistical analysis

Starting from a series of 3D tomographic images recorded in the micro shear-tester, we aimed to extract as much information on particle level as possible. For method development, we focused on a shear experiment with spherical particles (BSGMS 27-32  $\mu\text{m}$ , CoSpheric LLC, USA; abbreviated BSGMS) with a diameter of roughly 30  $\mu\text{m}$ . The size distribution and an SEM image of several particles are shown in Fig. 3. However, many of the developed methods are also applicable to other particle sizes, shapes or materials. The experiment we studied was conducted quasi-statically with a normal load of 0.5 kPa. Particles were sieved into the sample chamber and the normal load was applied. Next, the sample was sheared, first in steps of  $0.5^\circ$  up to a cumulative shearing angle of  $9.5^\circ$ , then further in steps of  $5^\circ$  up to an overall angle of  $39.5^\circ$ . Directly after applying the normal load and after each step of shearing, a tomographic 3D image of the entire sample chamber was recorded. The experiment and analysis methods described in this section were previously published in [Han16,Han17].

First, the particles were segmented by applying a marker-based watershed transformation. Markers were chosen as the local maxima of the convolution of the original image with an idealized particle mask as suggested in [Wen13]. This approach is ideal for spherical particles with a narrow size distribution and also allowed for the correct segmentation of hollow particles

in most cases, which were occasionally present in the sample. Based on the segmentation, we could extract the center of mass and other geometric characteristics (e.g. diameter, volume, sphericity) for each particle. The main steps of particle segmentation are visualized in Fig.3.

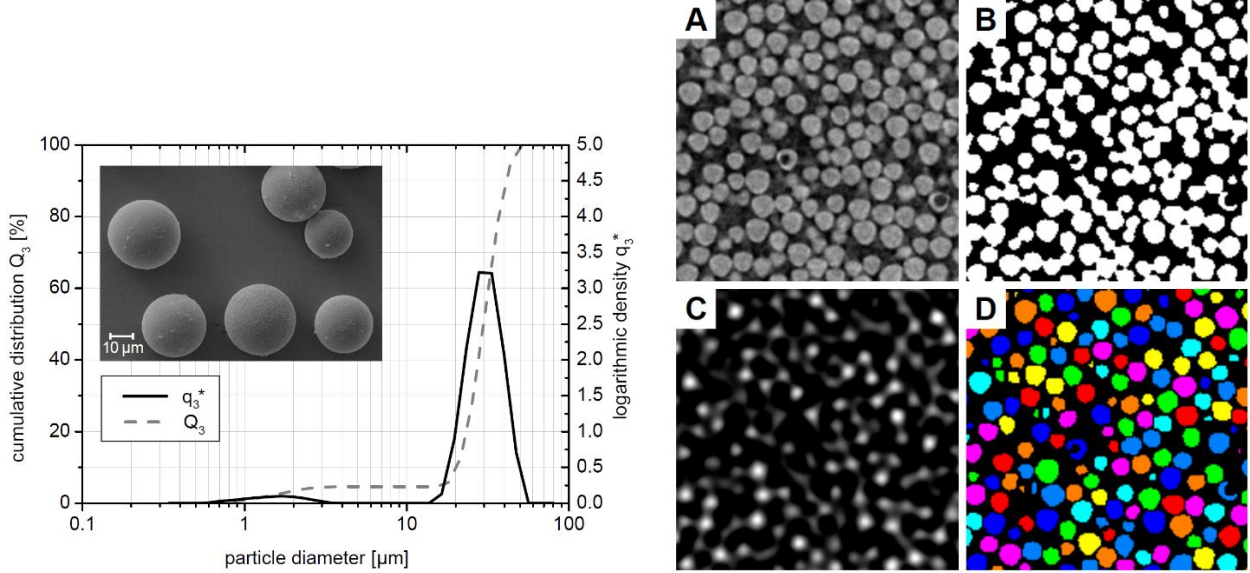


**Fig. 3** Left: Particle size distribution (mass distribution, logarithmic density and cumulative distribution function) and SEM picture (inset) of BSGMS glass particles. Right: Visualization of the main steps of the segmentation process based on a small cutout of an image slice. Grayscale image obtained by XMT (A), binary image (B), convolution of grayscale image and particle mask used for marker selection (C) and final segmentation result after applying the marker-based watershed transform (D). Note that though the visualization is in 2D, all operations are carried out in 3D. (Reprinted from [Han17] with permission from Elsevier)

Based on the extracted centers of mass, we computed tracks of particles over time. When shearing in steps of  $0.5^\circ$ , a comparatively simple algorithm was sufficient, which aims to minimize the sum of squared displacements in each step [Cro96]. In these small steps, particles are expected to move at most  $8.72 \mu\text{m}$  (at the upper outer edge of the cylindrical sample chamber), which is less than a particle radius. When larger angle increments of  $5^\circ$  are used between tomographic images, this approach is no longer feasible.

We solved this problem by deriving a first estimation of the average movement of particles in different areas of the shear cell directly from the 3D image data, extending an idea from [Str14b]. Here, an image-based local shear deformation was computed by comparing image slices at two consecutive points in time and a fixed height,  $z$ . For a time step  $(t_1, t_2)$  the local angle of shear deformation  $\Delta_\varphi^{t_1 \rightarrow t_2}$  at height  $z$  was then defined as the angle by which the first slice has to be rotated to best match the second slice. More precisely,

$$\Delta_\varphi^{t_1 \rightarrow t_2}(z) = \operatorname{argmax}_{\alpha \in [0^\circ, 360^\circ]} \{ \operatorname{corr}(\operatorname{rot}_\alpha(I_{t_1}^z), I_{t_2}^z) \}, \quad (1)$$

where  $I_t^z$  denotes the image slice at time  $t$  and height  $z$ ,  $\text{corr}$  denotes the image cross-correlation, and  $\text{rot}_\alpha$  denotes the rotation around the image center by the angle  $\alpha$ . The image rotations were implemented using bilinear interpolation and maximization was carried out in steps of  $0.1^\circ$ . We extended this approach to capture also radial variations of local shear deformation and to measure vertical compression or dilation along with the rotational deformation. For this purpose, we divided each image slice into  $k$  disjoint, concentric rings  $R_1, \dots, R_k$  with equal area and maximized image cross-correlation with the corresponding rings of the next time point while simultaneously applying a rotational and a translational deformation. Note that each ring is rotated independently and shifted vertically now, not the image slice as a whole. This yields the 2D optimization problem

$$\left( \Delta_\varphi^{t_1 \rightarrow t_2}(z, r_i), \Delta_z^{t_1 \rightarrow t_2}(z, r_i) \right) = \underset{\substack{\alpha \in [\alpha_{\min}, \alpha_{\max}] \\ h \in [h_{\min}, h_{\max}]}}{\text{argmax}} \{ \text{corr}(\text{rot}_\alpha(I_{t_1}^{z, R_i}), I_{t_2}^{z+h, R_i}) \}, \quad (2)$$

where  $i \in \{1, \dots, k\}$ ,  $r_i$  is the central radius of ring  $R_i$ , and  $I_t^{z, R_i}$  denotes ring  $i$  on the image slice at time  $t$  and height  $z$ . We used  $k = 10$  rings and chose the range for the optimization of the vertical deformation based on the sizes of the 3D image stacks in  $z$ -direction,  $z_{\max}^{t_1}$  and  $z_{\max}^{t_2}$ , as

$$[h_{\min}, h_{\max}] = [\min\{z_{\max}^{t_2} - z_{\max}^{t_1}, 0\}, \max\{z_{\max}^{t_2} - z_{\max}^{t_1}, 0\}]. \quad (3)$$

To speed up calculations,  $\alpha$  was not optimized over the full range of  $360^\circ$  but was restricted to a realistic range, where  $\alpha_{\min} = -1^\circ$  and  $\alpha_{\max}$  was set to the actual angle of shearing applied to the sample between times  $t_1$  and  $t_2$  plus  $1^\circ$ . Using bilinear interpolation in the coordinates  $z$  and  $r_i$ , this method can be used to obtain an estimate of the local shear deformation at any location in the sample. A similar approach can also be used to measure the rotation of upper and lower piston (see Section 4). We will refer to the left-hand sides of Eq. 1 and 2 as 1D and 2D image-based local shear deformation, respectively. An example for the results of the image-based local shear deformation is shown in Fig. 4.

We used the 2D image-based local shear deformation as prior information for tracking particles in shearing steps of  $5^\circ$ . For each particle at time  $t_1$  we computed the hypothetical position where it would be expected at time  $t_2$  if it perfectly followed the average movement summarized in the image-based local shear deformation. Then, instead of minimizing the sum of squared displacements, we minimized the sum of squared distances between hypothetical and actual particle positions at time  $t_2$ . In both cases, with the simple algorithm for steps of  $0.5^\circ$  and the adapted one for steps of  $5^\circ$ , optimization was carried out on a reduced problem as suggested in [Cro96], discarding possible assignments if the displacement (or distance between hypothetical and actual position) exceeded a predefined threshold.

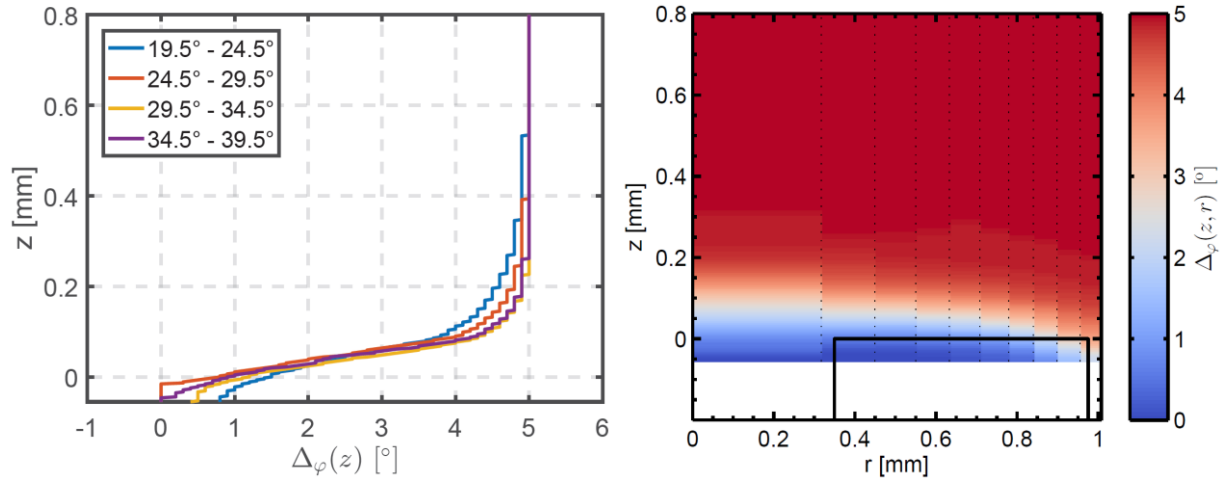


**Fig. 4** Image-based local shear deformation in 1D and 2D in the steady state of the experiment. The 1D case (left) shows the shear deformation as a function of the height in the sample with almost congruent states. The 2D deformation, which is shown for the last time step as an example (right), reveals that the shear band geometry is curved close to the wall. (Reprinted from [Han17] with permission from Elsevier)

Using this approach, we computed a particle tracking for all steps starting at  $\omega t = 3.5^\circ$ . In previous time steps, the distance between upper and lower piston decreased considerably, from 2.12 mm to 1.93 mm, leading to large vertical displacements of particles. This densification was spatially inhomogeneous, even in  $\varphi$ -direction, so that it could not be estimated with the 2D image-based local shear deformation and reliable tracks could not be identified. In all other time steps, we achieved tracking efficiencies of at least 99.5% for angle increments of  $0.5^\circ$  and at least 97% for angle increments of  $5^\circ$ . Here, tracking efficiency is defined as the percentage of particles in the segmented image, which were successfully assigned to a particle track. We additionally validated our algorithm for tracking in steps of  $5^\circ$  using the first part of the experiment, where image data in steps of  $0.5^\circ$  is available. When comparing the results of the  $5^\circ$ -step tracking (without considering intermediate time points) and the  $0.5^\circ$ -step tracking (using all available time points), we could show that more than 98.5% of the identified tracks were identical.

Based on the particle tracking, we first computed absolute particle velocities, measured as the distance a particle traveled in a time step per degree of shearing ( $\mu\text{m}/^\circ$ ). Particle velocities on the same height but at two different points in time are visualized in Fig. 5. As clearly visible in this figure, the axis of rotation does not always perfectly coincide with the central axis of the cylindrical sample chamber. This may be caused by small inaccuracies in the alignment of the upper and lower piston and the glass capillary. Since assuming a wrong axis of rotation would have led to significant errors in angular velocities, which are of major interest for shear band analysis, we estimated the actual axis of rotation from the data. This was achieved by fitting circles to particles with approximately the same height and absolute velocity at each time point using weighted least squares, and averaging the circle centers estimated at each  $z$ -coordinate. Note that the resulting estimated axis of rotation is not necessarily a straight line but may be

curved. Since no rotation occurs at the bottom of the sample, all particles at this height have velocities close to zero and fall into the same velocity class, so the estimated axis of rotation will automatically be close to the center of the sample chamber in this region.

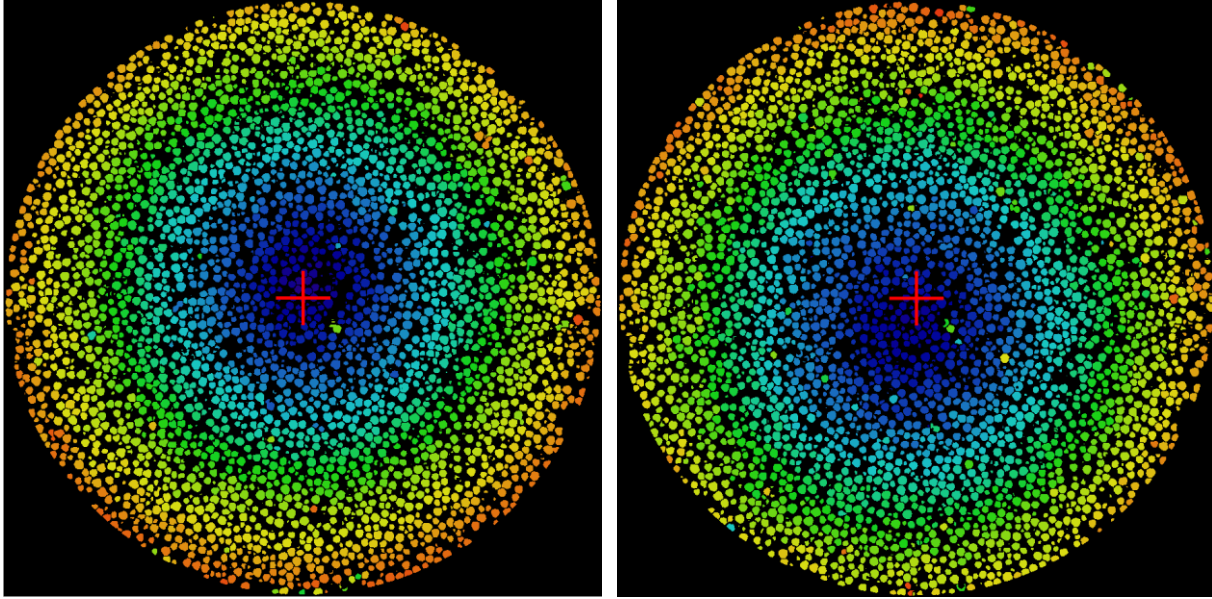


**Fig. 5** Slice of the binary image at two different points in time. Each particle is colored according to the distance it travels in the subsequent time step, blue indicates small and red indicates large values. In the first time step (left) the center of rotation is slightly above and in the second time step (right) it is below and left of the center of the sample. The image centers are marked with a red cross. (Reprinted from [Han17] with permission from Elsevier)

### 2.3 Discrete element method: Contact force models and boundary conditions

The simulations reported here are done with the discrete element method (DEM) using soft spherical particles, i.e. all particle trajectories are calculated by numerically solving Newton's equation of motion. Particles interact via pairwise forces and torques, dictated by the chosen contact model, which is a function of the particle diameters ( $d_i, d_j$ ), their relative position ( $\vec{r}_{ij} = \vec{r}_i - \vec{r}_j$ ), velocity, angular velocity, and their contact history to account for friction. As usual, normal ( $F_n = \vec{F}_{ij} \cdot \vec{r}_{ij} / |\vec{r}_{ij}|$ ) and frictional forces are treated separately [Lud08]. For the normal contact force three different models will be discussed in detail below. Coulomb friction, as well as rolling and torsional friction (in case of 3D simulations) are implemented with a model similar to the one presented in [Lud08]: Each contact mobilization mode (sliding, rolling and twisting) is suppressed individually by using a linear spring-dashpot model until a particular threshold is exceeded. This threshold as well as the friction force and torque, when a contact is mobilized are proportional to the absolute value of normal plus adhesion force  $|F_n + F_{adh}|$ .

### 2.3.1 Contact model for 2D caking simulations

To understand, how the contact accommodation time  $t_c$  affects the bulk's rheology, we use 2D simulations and a simple linear spring-dashpot model. Hence, particles experience a viscoelastic force, which increases linearly with their overlap  $\xi = (d_i + d_j)/2 - |\tilde{r}_{ij}|$  and their relative normal velocity  $\dot{\xi}$ . A contact is assumed to form, when  $\xi$  becomes positive, and to last (even for negative overlap, see Fig.6 (left)), until the normal force drops below a threshold  $-F_{adh}(t_k)$ , which depends on the contact's age  $t_k$ ,

$$F_{adh}(t_k) = F_{adh}^{(max)} \frac{4 r_{eff}}{\langle d \rangle} (1 - e^{-t_k/t_c}) . \quad (4)$$

While the contact exists, the adhesion force grows from zero to the saturation value  $F_{adh}^{(max)} 4 r_{eff}/\langle d \rangle$ . The parameter  $r_{eff} = 1/2 d_i d_j / (d_i + d_j)$  denotes the reduced radius, and  $\langle d \rangle$  the average particle diameter.  $F_{adh}^{(max)}$  is a given constant. This age dependence of the adhesion force is inspired by the formation of solid bridges between particles (see [Tom97, Weu15]). With respect to the average contact time, which in case of quasi-static deformations is approximately given by the inverse shear rate  $\dot{\gamma}^{-1}$  [Weu17], two regimes can be identified. If  $t_c \ll \dot{\gamma}^{-1}$ , the maximum adhesion force acts immediately as soon as the contact is established, defining an *adhesion dominated* flow regime. For  $t_c \gg \dot{\gamma}^{-1}$ , no significant adhesion force is built up during the duration of a contact, and the bulk's behavior is determined by the preparation procedure prior to the shear, defining a *cementation dominated* regime [Cuc99, Weu13]. The theoretical results for the whole range of the dimensionless parameter  $\dot{\gamma}t_c$  will be discussed in Section 3.

These simulations were done for plane shear under constant normal load  $P$ . The coordinate system was chosen such that  $x$  is the direction of shear and  $y$  the direction of normal pressure. Periodic boundary conditions were used in  $x$ -direction. In order to study shear banding in the bulk without perturbations by walls [Rie17,Rog15,Sho12a,Sho12b], Lees-Edwards boundary conditions [Cam05] were implemented in  $y$ -direction. However, in order to account for the non-affine nature of quasistatic shear [Fen04,Tig12], we refrained from prescribing a homogeneous shear deformation. As we are interested in shear-banding rather than calculating linear transport coefficients, we induce the deformation purely by the boundaries in  $y$ -direction. Hence, these boundaries become well defined layers in space and break translational invariance in  $y$ -direction (see also [Sod03]). The normal load  $P$  was regulated to a constant value by a variable system height. It responded to a deviation of the stress component  $\sigma_{yy}$  from the desired value  $P$  with a rate proportional to  $(\sigma_{yy} - P)/P$ . The corresponding control constant was set larger than  $20 \cdot \dot{\gamma}$  to assure constant pressure during shear deformation. Following [MiD04], we used a shear rate of  $\dot{\gamma} = 5 \cdot 10^{-4} \sqrt{P/m}$  with  $m$  being the average particle mass, which in the adhesion dominated flow regime can be regarded as quasi-static deformation.

We used the normal load  $P$ , the particle diameter average  $\langle d \rangle$  and the particle mass density  $\rho$  as natural units. To avoid crystallization effects, a moderate polydispersity was utilized by evenly distributed particle diameters  $0.5 \leq d/\langle d \rangle \leq 1.5$ . Table 1 summarizes the parameter choice, where the same notation as in [Lud08] was used.

**Table 1:** Parameters for 2D simulations

Parameter	$k_n/P$	$\frac{\gamma_n}{\sqrt{k_n m_{\text{eff}}}}$	$k_t, k_r$	$\frac{\gamma_t}{\sqrt{k_t m_{\text{eff}}}}$	$F_{\text{adh}}^{(\text{max})}/P\langle d \rangle$	$\mu$	$\mu_r/r_{\text{eff}}$
Value	$10^5$	1	$k_n/2$	2	10	0.5	0.1

### 2.3.2 Contact model for micro-sized glass beads

Micro-sized borosilicate glass particles at room temperature serve as a model material for the limit  $\dot{\gamma}t_c \rightarrow 0$ . Experimental results will be analyzed in Section 4. They compare favorably [Tor17] with simulations done with the contact model described in the following:

Due to the spherical shape of the glass particles, modelling demands a Hertzian contact model. While literature offers a variety of sophisticated contact models for spherical particles, which include elastoplastic response [Tho98, Tom97] or different formulations of the damping term [Ant11, Bri96], we intentionally keep the model as well as the parameter choice as simple as possible. For the normal part of the contact force, we use the viscoelastic model combined with a non-zero, constant adhesion force  $F_{\text{adh}}$  for positive overlap,

$$F_n(\xi, \dot{\xi}) = \left( \frac{4 E_{\text{el}} \sqrt{r_{\text{eff}}}}{3} \xi^3 + \gamma_n \sqrt{\xi} \dot{\xi} - F_{\text{adh}} \frac{r_{\text{eff}}}{\langle r_{\text{eff}} \rangle} \right) \theta(\xi) , \quad (5)$$

with the effective elastic modulus  $E_{\text{el}}$ , a viscosity coefficient  $\gamma_n$  and the Heaviside function  $\theta(\xi)$ . The particle stiffness and adhesion force are set according to the experimentally determined values. Tangential stiffness is set to  $k_t = 2/7 k_n$  with  $k_n = 4/3 E_{\text{el}} x_{50,2}/2$  (see [Tor17] for details). In the quasi-static deformation regime, viscous forces play a minor role [MiD04], so that one is free to enforce a high dissipation rate by setting  $\gamma_n = \sqrt{4/3 E_{\text{el}} m_{\text{eff}}}$ , where  $m_{\text{eff}}$  is the reduced mass. The same argument applies to Coulomb friction implemented by damped linear springs with a damping constant of  $2\sqrt{k_t m_{\text{eff}}}$ . The torsion friction coefficient is linked to the Coulomb friction coefficient by setting  $\mu_{\text{tor}} = r_{\text{eff}} \mu$ , and we employ a load dependent rolling friction coefficient  $\mu_{\text{rol}} = \sqrt{2 r_{\text{eff}} \xi}$ . The Coulomb friction coefficient is calibrated by comparing the macroscopic friction coefficient of plane shear simulations under a constant normal load of  $\sigma = 5$  kPa with the experimental findings [Tor17].

### 2.3.3 Elastoplastic contact model for potassium chloride

Micro-sized KCl particles serve as model material for the limit  $\dot{\gamma}t_c \rightarrow \infty$ . It shows load dependent caking on a time scale of 10 – 20 min. For this material we developed a protocol that allows a complete calibration (and independent validation) of an elastoplastic contact model, based on nanoindentation results and macroscopic shear experiments as described in [Weu15]. Here, just a brief explanation of the main concepts will be given.

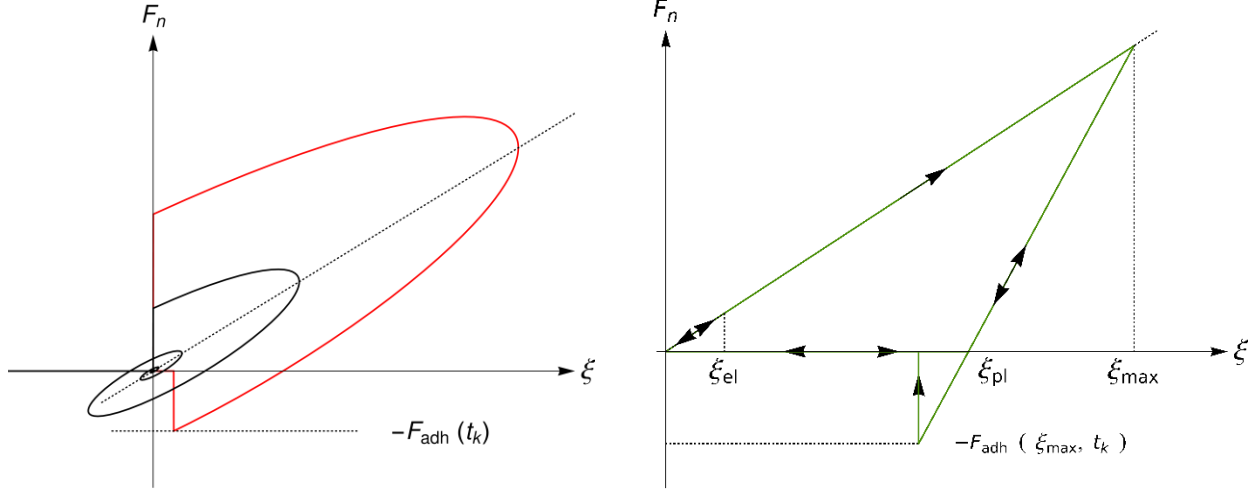


**Fig. 6** Left: Normal force of the linear viscoelastic contact model with time dependent adhesion, see Section 2.3.1. Collision with adhesive capture (black), or with particle bounce back (red). Right: Elastoplastic contact model with time dependent adhesion, see Section 2.3.3, suited for potassium chloride (Reprinted with permission from [Weu17]).

Although the KCl particles have facets with rounded edges, they are represented as spheres in the simulation. Nanoindentation experiments reveal an approximately piecewise linear relation [Weu15] between the contact force and the particle deformation that is represented in the simulation model by the overlap  $\xi$  between the particles. Fig. 6 (right) depicts the idealized normal force between two colliding particles as a function of their overlap. It consists of a loading branch, which apart from an initial small elastic part describes plastic deformation at yield stress  $\sigma_{pl}$ , and an elastic unloading / reloading branch governed by an effective elastic modulus  $E_{el}$ . For dimensional reasons, the two linear branches must have the form

$$\begin{aligned}
 F_n(\xi) &= \sigma_{pl} L_{pl} \xi && \text{for loading,} \\
 F_n(\xi) &= E_{el} L_{el} (\xi - \xi_{pl}) && \text{for unloading,}
 \end{aligned} \tag{6}$$

where  $\xi_{pl}$  is the residual plastic deformation after complete unloading. The length scales  $L_{pl}$  and  $L_{el}$  characterize the geometry, while the stress scales are material constants, and the overlap stands for the deformation. For undeformed spheres the only length scale is the radius, hence  $L_{pl} \propto r_{eff}$ . However, the unloading takes place at an irreversibly flattened contact area after plastic deformation. Hence, in addition to  $r_{eff}$ , the contact geometry depends also on the maximum overlap  $\xi_{max}$ . Guided by the scaling of the radius of the circular contact area of overlapping spheres, we postulate  $L_{el} \propto \sqrt{r_{eff} \xi_{max}}$ . Because of the scaling of the unloading stiffness with the square root of the maximum overlap, a realistic velocity dependence of the restitution coefficient can be expected [Tho17].

Due to adhesion, the elastic branch persists at tensile forces, as long as the threshold  $-F_{adh}$  is not exceeded, at which the contact opens abruptly. The threshold combines a cementation as well as an adhesive component phenomenologically:

$$F_{\text{adh}}(t_k) = \sigma_{\text{adh}} A_{\text{adh}} e^{-t_k/t_c} + \sigma_{\text{cem}} A_{\text{cem}} (1 - e^{-t_k/t_c}), \quad (7)$$

i.e. contact crystallization leads to a replacement of the adhesive part  $\sigma_{\text{adh}} A_{\text{adh}}$  by a cementation term  $\sigma_{\text{cem}} A_{\text{cem}}$  on a timescale  $t_c$ . We find that the bulk's load dependence in the adhesive limit is best described by  $A_{\text{adh}} = \chi_{\text{adh}} r_{\text{eff}}^2 (1 + \xi_{\text{max}}/r_{\text{eff}})$  and leave  $\sigma_{\text{adh}} \chi_{\text{adh}}$  as a calibration parameter [Weu15, Weu17]. The tensile strength in the cementation limit is given by the plastic yield stress of KCl and a load dependent contact area  $A_{\text{cem}} = \chi_{\text{cem}} r_{\text{eff}} \xi_{\text{max}}$ , where  $\sigma_{\text{cem}} \chi_{\text{cem}}$  is used as a fit parameter.

The materials yield stress was determined with nanoindentation tests. Furthermore, we assumed the unloading and reloading branch to be viscoelastic and included a moderate damping coefficient. As in Section 2.3.2, torsion friction is linked to Coulomb friction. The influence of particle shape was taken into account by a rolling friction coefficient that was determined with SEM images and an approach presented in [Est11]. The Coulomb friction coefficient  $\mu$ , as well as the parameters for tensile forces  $\sigma_{\text{adh}} \chi_{\text{adh}}$  and  $\sigma_{\text{cem}} \chi_{\text{cem}}$  were calibrated by comparing the stress response in plane shear experiments and simulations.

### 2.3.4 Boundary conditions

Calibration of the contact models (Sections 2.3.2 and 2.3.3) was done by wall-driven plane shear simulations. Specifically, frictional walls structured by vanes (see Fig. 1 (right)) and periodic boundaries in the directions perpendicular to  $y$  were used. The motion of the upper wall was velocity controlled in shear direction and force controlled in  $y$ -direction.

Simulations of the micro-shear tester [Tor17] were done with the same torsional shear cell geometry but a slightly smaller diameter (1.78 mm), i.e. a cylinder for particle confinement in horizontal direction and two structured pistons (one movable, one fixed) in vertical direction. Since we neglect plastic deformation, a small gap of 0.1 mm between the outer edge of the piston and the cylinder wall was introduced to avoid jamming of single particles. Particle-wall interaction is described by the viscoelastic part of the contact model in Eq. 5, using the same material parameters.

## 3 Rheology of caking granular matter: A 2D simulation study

Here we answer the fundamental question, how a finite contact accommodation time  $t_c$  affects rheology. The simulations are performed in 2D with the contact force model described in Section 2.3.1. The results are compared with theoretical predictions obtained from the principle of minimal energy dissipation. Starting point is always a completely accommodated bulk, i.e.  $t_k/t_c \rightarrow \infty$  in Eq. 4. Depending on the dimensionless parameter  $\dot{\gamma} t_c$ , qualitatively different shear heterogeneities emerge. As the average contact time is given by the inverse shear rate,  $\dot{\gamma} t_c$  characterizes the competition between opening and forming of caked contacts. For  $\dot{\gamma} t_c \ll 1$ , we expect the behavior of a normal cohesive granular bulk, while  $\dot{\gamma} t_c \gg 1$  defines the *cementation dominated regime* where adhesion forces vanish, when a contact fails, and never recover to their former value, because the contacts don't live long enough. Therefore, shear banding in the cementation dominated regime is conceptually similar to fracture. Upon further

shear, the initial crack is expected to widen, grinding up the adjacent caked material. This mechanism needs to be understood first, because it is at the core of the rheology of caking granular matter.

Inspired by the sample preparation in common shear tests [Sch03, Sch09], we prepare a well-defined, reproducible initial state by driving the cohesive bulk, setting  $t_c = 0$ , into steady state shear [Rot04, Woo90]. This choice avoids over-consolidation and hence the resulting dilatancy under shear, for all  $t_c > 0$ , as the same normal pressure  $P$  is applied for preparation and shear simulations. Different (average) system heights were implemented at a fixed system width ( $= 88 \langle d \rangle$ ) in shear direction, in order to check finite size effects for the shear bands. System size is given in terms of total particle number  $N$ .

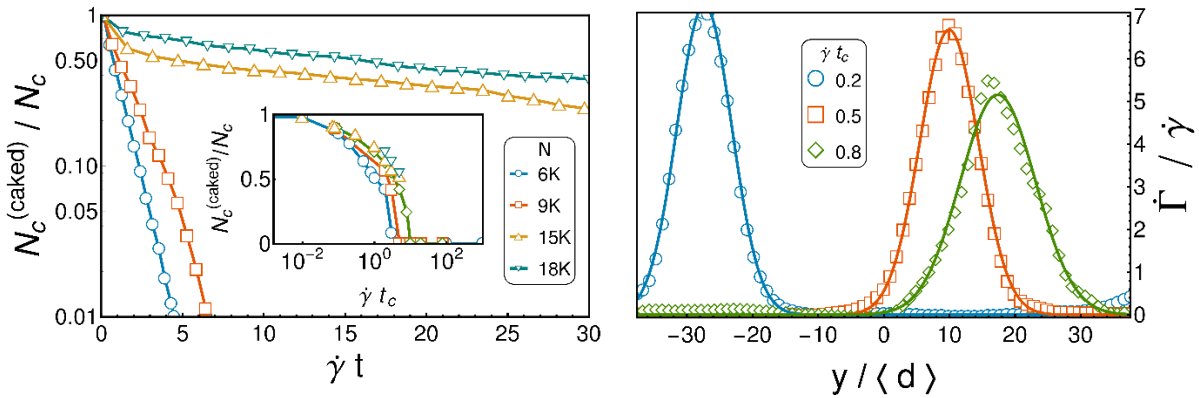


**Fig. 7:** Portion of caked contacts as a function of shear deformation for  $\dot{\gamma} t_c = 80$  (left) and as a function of  $\dot{\gamma} t_c$  after a total shear deformation of  $\dot{\gamma} t = 30$  (inset). Snapshots of the local shear rate as a function of  $y$ , fitted by Eq. 8 (right). (Reprinted with permission from [Weu17])

Fig. 7 (left) illustrates for  $\dot{\gamma} t_c = 80$  and different system sizes, how the initially caked configuration is ground up in the cementation dominated regime. We call contacts caked, if they have existed longer than the accommodation time  $t_c$ . Their number decreases roughly exponentially within the simulated time span. The two small systems ( $L_y/L_x \lesssim 1$ ) lose all caked contacts and become a homogeneously sheared, weakly cohesive material on a timescale  $\dot{\gamma}^{-1}$ . There is a qualitative difference compared to the two larger systems, where the timescale of the exponential decay of caked contacts is approximately  $t_c = 80\dot{\gamma}^{-1}$ , instead.

We repeated this kind of simulation many times for a whole range of  $\dot{\gamma} t_c$ -values and system sizes. Evaluating only those runs, which reached a steady state by the time  $t \approx 30\dot{\gamma}^{-1}$ , the fraction of contacts with  $t_k > t_c$  is shown in the inset of Fig. 7 (left). In the adhesion dominated regime ( $\dot{\gamma} t_c \ll 1$ ), we observe no structural or mechanical change with respect to the initial configuration. Thus, the two limits of vanishing and infinite accommodation time tend towards the steady states of a cohesive or a non-cohesive bulk, respectively. In the intermediate regime between these limiting cases, the sheared system remains partially caked.

We examined this regime more closely by measuring the local shear rate  $\dot{\Gamma}(y) = \partial v_x / \partial y$ , which was calculated from the coarse-grained velocity field, averaged in  $x$ -direction. Shearing is localized between two caked slabs. The shear bands can be fitted by

$$\dot{\Gamma}(y) = \dot{\gamma} \frac{L_y}{\sqrt{2\pi} w_{sb} \operatorname{erf}(L_y/2\sqrt{2}w_{sb})} e^{-\frac{(y-y_{sb})^2}{2w_{sb}^2}}, \quad (8)$$

as displayed in the right graph of Fig. 7. As the averaged contact time within these shear bands is less than  $t_c$ , adhesion forces are suppressed, which is why the shear bands turn out to be more densely packed than the average bulk [Weu17]. Because of shear weakening due to reduced adhesion inside the shear band, its position  $y_{sb}$ , once established randomly, is rather stable. Only rare spontaneous jumps of the position were observed.

In the following we will present a qualitative explanation for these shear heterogeneities based on the principle of minimal energy dissipation [Ons31a,Ons31b] which was previously used in the context of granular matter for the prediction of shear band configurations [Moo13,Ste11,Ung04]. Under the assumption that the work done is fully dissipated, the dissipated power density equals the product of shear stress  $\tau$  and shear rate  $\dot{\gamma}$  [DaC05]. For dense granular flow the shear stress depends on the shear rate in the following way:

$$\tau(\dot{\gamma}) = \tau_{\min}(\eta) + b(\eta) \sqrt{mP} \dot{\gamma}, \quad (9)$$

where the threshold  $\tau_{\min}(\eta)$  as well as the coefficient  $b(\eta)$  are functions of the dimensionless cohesion number  $\eta = F_{\text{adh}}/Pd$  [Rog08]. According to Eq. 4 one must consider a local cohesion number, which depends on the average lifetime of contacts

$$\eta = \eta_{\max} (1 - e^{\langle t_k \rangle / t_c}). \quad (10)$$

The combination of Eq. 5 and 9 yields to first order in  $\eta$

$$\tau(\dot{\gamma}) = \tau_0 + \tau_1 (1 - e^{\langle t_k \rangle / t_c}) + (b_0 + b_1 (1 - e^{\langle t_k \rangle / t_c})) \dot{\gamma}. \quad (11)$$

The constants  $\tau_0$  and  $\tau_1$  were measured in simulations of the steady state flow of the adhesion dominated limit.  $b_0$  and  $b_1$  can be estimated with literature values [Rog08]. To proceed further, we switch to the concept of local rheology. By neglecting the time dependence of the local shear rate, we assume translational invariance in shear direction and set  $\langle t_k \rangle = \langle t_k \rangle(y) = 1 / \dot{\Gamma}(y)$ , hence the contact time of each layer within the bulk is proportional to the inverse local shear rate. Combining these equations, we get the dissipation rate

$$\dot{E}_{\text{dis}}[\dot{\Gamma}] = L_x \int_{-L_y/2}^{L_y/2} \tau(\dot{\Gamma}(y), \eta(\dot{\Gamma}(y), t_c)) \dot{\Gamma}(y) dy, \quad (12)$$

as a functional of the local shear rate  $\dot{\Gamma}$ . Inserting Eq. 3 for  $\dot{\Gamma}(y)$ , the dissipation rate becomes a function of shear band width and accommodation time  $\dot{E}_{\text{dis}}(w_{sb}, t_c)$ . In the limits  $t_c \rightarrow 0$  and  $t_c \rightarrow \infty$  this function can be calculated analytically. For finite  $t_c$  the dissipation rate is determined by

numerical integration (Fig. 8, left). In the cementation as well as in the adhesion dominated regime, the dissipation rate decreases monotonically as a function of shear band width. Hence, the theory predicts  $w_{sb} \rightarrow \infty$  as the state of least dissipated power and therefore homogenous shear. However, for intermediate values of  $\dot{\gamma} t_c$ , a local minimum at finite  $w_{sb}$  exists, and the state of least energy dissipation predicts inhomogeneous flow and shear bands. The right graph in Fig. 8 shows the measured shear band width (median) as a function of  $\dot{\gamma} t_c$  (symbols) as well as the predicted  $w_{sb}$  utilizing Eq. 12 for various system sizes  $L_y$ . (Shaded areas quantize fluctuations when fitting Eq. 8.) As predicted by theory, simulation results confirm shear zones with finite  $w_{sb}$ , which increases sub-linearly as a function of  $\dot{\gamma} t_c$ . As we argued in the framework of a local rheology, it is not surprising, that theory underestimates the measured shear band width (see e.g. [MiD04] or [Rie16] for a more detailed discussion). Still the functional dependence in the regime  $\dot{\gamma} t_c \approx 1$  is captured qualitatively correct. Furthermore, within the framework of a local rheology, the finite shear-band width is predicted as another length scale besides the particle diameter.

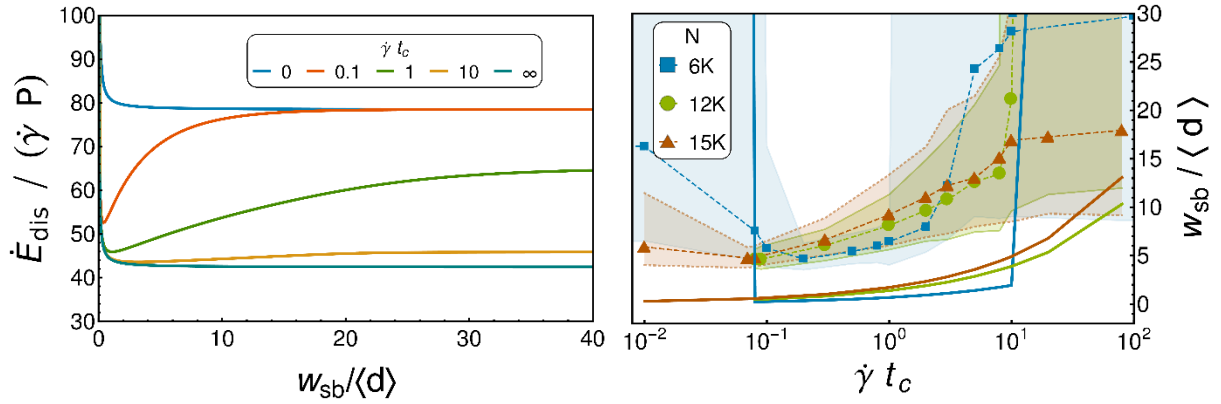


**Fig. 8:** Dissipation rate as a function of shear band width for different  $\dot{\gamma} t_c$  (left). Median of measured shear band width together with interval between quantiles 0.1-0.9 as shaded region, and the theoretical prediction according to Eq. 12 as solid lines (right). (Reprinted with permission from [Weu17])

#### 4 Complex shear localization in the micro-shear tester

We analyzed the experiment described at the beginning of Section 2.2 to assess shear induced structural heterogeneity as well as shear band formation and evolution over time. This was a micro-sized torsional shear experiment with spherical glass particles and a constant normal load. As the cohesion forces between particles are small compared to the normal stress ( $\eta = F_c / (\sigma x_{50,3}^2) \approx 0.2$ ), they are expected to have only a minor influence. A total shear strain of  $\omega t = 39.5^\circ$  was analyzed based on tomographic images, which were taken in steps of  $0.5^\circ$  degrees for the first  $9.5^\circ$  of shearing, and in steps of  $5^\circ$  for the remaining experiment. The results summarized in this section were previously published in [Han16,Han17].

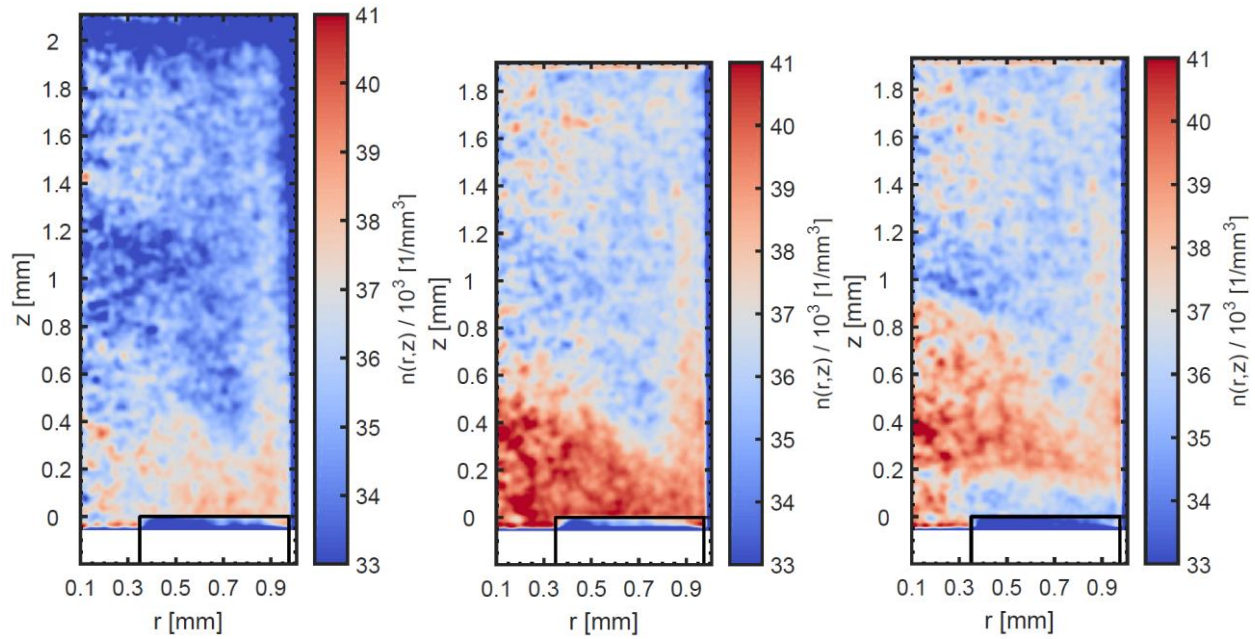


**Fig. 9** 2D density profiles (coarse-graining length  $w = 14.9 \mu\text{m}$ ) of the initial configuration ( $\omega t = 0^\circ$ ; left), a compacted configuration ( $\omega t = 4^\circ$ ; center) and a configuration towards the end of the experiment  $\omega t = 34.5^\circ$ ; right). The black frame in the bottom right corner marks the location of the vanes on the lower piston. (Reprinted from [Han17] with permission from Elsevier)

We first analyzed the spatial structure of the sample and its evolution over time. Particles were segmented in all tomographic images as detailed in Section 2.2 and the centers of mass were computed based on their voxel representations. Extremely small and extremely large particles were excluded since they likely occur due to artifacts or segmentation errors, though the volume of excluded particles was less than 0.1% of the sample volume at all time points. Based on the extracted centers of mass, we computed the number density, i.e., the expected number of particles per cubic millimeter, as a function of height ( $z$ ) and radial coordinate ( $r$ ). We coarse-grained the data with a Gaussian kernel with standard deviation  $w$  to obtain continuous fields and averaged over  $\varphi$ , assuming rotational invariance. Fig. 9 shows the number density profiles for the initial configuration, a consolidated configuration and a configuration towards the end of the experiment. The profiles reveal that the sample is compressed during the first steps of shearing ( $\omega t = 0^\circ$  to  $\omega t = 4^\circ$ ) and that the number density is larger in the bottom of the sample than on top. The compression and low density at the top of the sample indicate that applying the uniaxial normal load after sieving the particles into the sample chamber is not sufficient to spread the particles on top out evenly. This process is completed during the first steps of shearing. Moreover, Fig. 9 shows that there is an almost cone-shaped, denser zone in the lower center of the shear cell. This might also be caused by the preparation procedure, e.g. by particles piling on top of each other at the beginning of sieving, which are later compressed by other particles on top. However, this interpretation needs further investigation. A dilation can only be observed after  $\omega t = 4^\circ$  and occurs directly above the lower piston, suggesting that this is the location of the shear zone.

In addition, we computed particle tracks, estimated the axis of rotation from the data and computed angular velocities of all particles with respect to this estimated axis as described in Section 2.2. We also used the 1D image-based local shear deformation (see Section 2.2) to accurately measure the movements of upper and lower piston by maximizing image cross-correlation in slices where the pistons are visible using a very small step size of  $0.01^\circ$ . In principle, this movement should be exactly as dictated by the experiment, i.e.,  $0.5^\circ$  or  $5^\circ$  per step for the upper piston and no movement for the lower piston. However, we measured deviations from this ideal, mostly at the lower piston. The mean absolute differences between target and actual movements were  $0.02^\circ$  and  $0.19^\circ$  at the upper and lower piston, respectively. The reason for this deviation in rotational movement probably lies in the experimental setup. The compensation unit tracks shear stress and is supposed to keep the lower piston in place, but particles interlocked between piston and wall might counteract this mechanism so that the lower piston gets partially dragged along. This problem could be solved by increasing the gap between lower piston and wall, yet this would simultaneously lead to more loss of sample material, which might be pushed out of the sample chamber through the gap. Moreover, only the rotation of the upper piston and glass capillary can be controlled in the micro shear-tester. Rotations of the lower piston can unfortunately not be observed with an accuracy of  $0.01^\circ$  during shear deformation. To ensure comparability of angular velocities between time steps, we normalized them to the interval of  $[0,1]$  based on the movements of upper and lower piston measured in the image data.

We found that for a fixed radial distance from the axis of rotation, the normalized angular velocity profiles could well be described by the parametric function

$$v_\varphi(z) = \frac{1}{2} + \frac{1}{2} \operatorname{erf}\left(\frac{z-z_{sb}}{w_{sb}}\right), \quad (13)$$

where erf denotes the error function. The fitting parameters,  $z_{sb}$  and  $w_{sb}$ , can be determined with the least squares method and offer a quantitative description of the vertical location and width of the shear band (as a function of the radial coordinate). The parametric function given in Eq. 13 has previously been used in [Fen04] to describe a symmetric shear zone and is attractive because of its simplicity. We defined the shear band as the interval  $z_{sb} \pm w_{sb}$ , which covers roughly 84% of the velocity range in the data. Different choices to define shear band width would be possible, yet since we mainly want to quantitatively compare the experimental shear band characteristics between different time points, we stick to this simple choice. Fig. 10 shows examples of actual and fitted 1D velocity profiles for different radial coordinates and the time-averaged, coarse-grained ( $w = 14.9 \mu\text{m}$ ) 2D velocity profile after  $\omega t = 10^\circ$  with fitted shear band.

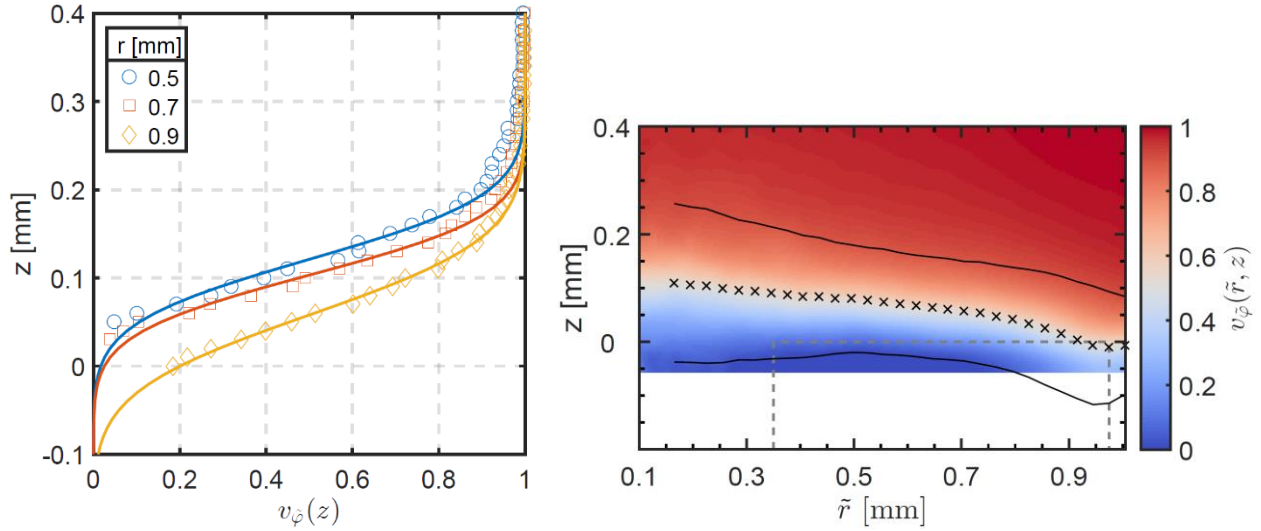


**Fig. 10** Example of actual and fitted velocity profiles for one time step ( $29.5^\circ$  to  $34.5^\circ$  of shearing) and different distances from the axis of rotation (left), and 2D velocity profile after  $\omega t = 10^\circ$  with the fitted shear band indicated in black as  $z_{sb} \pm w_{sb}$  (right). (Reprinted from [Han17] with permission from Elsevier)

The velocity profiles show that shear strain localizes directly above the lower piston, as was already indicated by the number density. Its center is at an average height of  $z = 0.12$  mm. The 2D profile additionally reveals that the shear band is slightly wider in the center of the shear cell and curved downwards near the cylinder wall. The latter is probably due to the fact that the outer cylinder wall rotates together with the upper piston, and particles close to it are more easily dragged along and achieve higher angular velocities than particles in the center. We observe an average shear band width of  $2w_{sb} = 250$   $\mu\text{m}$ , which corresponds to roughly 8 median particle diameters and agrees well with values reported in literature [Gou07, Guo12, Nem01, Str14b].

Using the parametric shear band representation, we analyzed the development of shear band width and location over time. A plot of  $z_{sb}$  and  $w_{sb}$  over time (averaged over the radial coordinate) is shown in Fig. 11. Shear band location and width fluctuate strongly at the beginning of the experiment, until a steady state seems to be reached at  $\omega t \approx 10^\circ$ . Lower fluctuations are expected after this point, since we implicitly average over much larger time intervals ( $5^\circ$  instead of  $0.5^\circ$  per step). In the initial phase of the experiment, the shear band is (on average) wider and rises from  $z_{sb} \approx 0.15$  mm to  $z_{sb} \approx 0.37$  mm before dropping back to its position right above the lower piston. Even in the more steady period after  $\omega t \approx 10^\circ$  the shear band width fluctuates perceptibly, taking values between  $w_{sb} \approx 0.8$  mm to  $w_{sb} \approx 0.16$  mm. There could be a second drop in variability at  $\omega t \approx 25^\circ$  but with the present data we cannot judge if the steady state is actually only reached at this point or if the second drop is merely a coincidence. Therefore, based on our analysis, we assume that the steady state is reached at  $\omega t \approx 10^\circ$ .

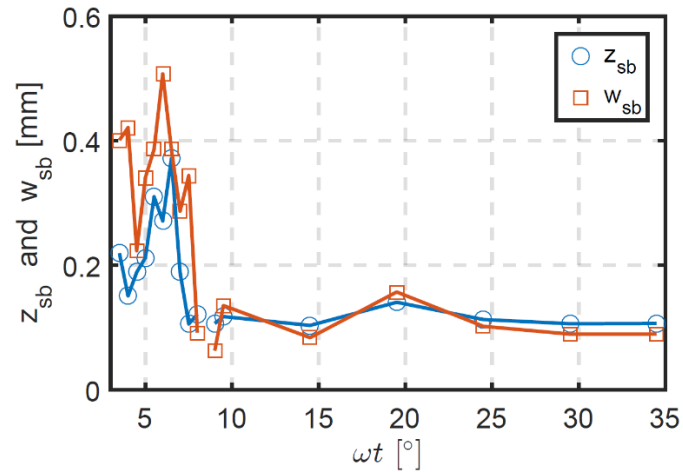


**Fig. 11** Development of the fitted shear band width and location over time, averaged over the radial coordinate. (Reprinted from [Han17] with permission from Elsevier)

## 5 Conclusion and Outlook

The interplay between particle contact properties, bulk structure and mechanical behaviour of fine, adhesive granular matter is of wide interest. In particular, time consolidation effects, i.e. time dependent adhesion, are far from being well understood, although they are of eminent importance for the handling of powders after storage. This chapter reviewed some recent progress in this respect.

Recording as much experimental information as possible on the particle motion during a shear experiment is vital for gaining insight into the relationship between bulk structure and mechanical behaviour. Ideally, observing the trajectory of every single particle offers information on local densification, loosening or formation of failure areas. Before we started our project this was only possible virtually by discrete element method (DEM) simulations.

We came very close to this ideal by developing a novel micro torsional shear tester which enables to measure yield loci of extremely small powder samples in the range of only 10  $\mu\text{l}$  with high accuracy in force and displacement measurements and which can be integrated into a high resolution X-ray tomography device ( $\mu\text{CT}$ ). Moreover, we developed the necessary statistical analysis methods which allow the extraction of the trajectories of almost all particles. The processing of time-resolved data makes it possible to localize and track particles despite large angle increments of up to  $5^\circ$  between tomographic measurements.

With this device and analysis tool stepwise compression and shear of powder samples were monitored in detail using particles in the size range between 10 and 100  $\mu\text{m}$ . In this chapter we reported results for two powder materials, borosilicate glass spheres and potassium chloride particles. The reason for this choice of model materials was that they represent very different particle contact properties, validated by simulations with the discrete element method (DEM). Contacts between the glass spheres could be described by a *viscoelastic* Hertz model shifted by

a *constant adhesion* force. Using a geometry comparable to the shear tester, the width and position of shear bands and the radial and axial particle density distribution could be reproduced.

Potassium chloride, on the other hand can be described by an *elastoplastic* model with a *time dependent adhesion* force that approaches a load dependent maximal value on a time scale of  $t_c \approx 15$  min, called accommodation time. A method to calibrate the DEM model was developed and proved. It is based on nanoindentation and shear tests. (This calibration strategy can also be applied to adhesion dominated materials, where  $t_c \approx 0$  .) After calibration, the simulation model could be independently validated.

For potassium chloride, accommodation happens very slowly compared to typical inverse shear rates, for the glass beads very fast. In this sense, the model materials represent extreme cases of cementation dominated, respectively adhesion dominated powders. In general, adhesive materials, when sheared, are expected to show behaviour in between these extreme cases. A systematic theoretical prediction of shear banding for finite accommodation times, and its qualitative support by DEM simulations has been given. The theory is based on the principle of minimal dissipation power and takes the shear weakening into account, which originates from the fact, that the average adhesion force reached during the lifetime of a particle contact decreases with increasing  $\dot{\gamma}t_c$ . Starting from a completely accommodated bulk, this leads to stable shear bands of finite width that increases with  $\dot{\gamma}t_c$ . Compared to the values obtained from simulation, the theory underestimates the shear band width. A possible reason is that the theory is based on local rheology. Creep effects are not taken into account. A nonlocal extension of the theory would be a promising future project.

## References

[Ant11] D. Antypov and J.A. Elliott, "On an analytical solution for the damped Hertzian spring," *Europhys. Lett.* **94**, 50004 (2011).

[Bri96] N.V. Brilliantov, F. Spahn, J.M. Hertzsch, and T. Pöschel, "Model for collisions in granular gases," *Phys. Rev. E* **53**, 5382 (1996).

[Cam05] C.S. Campbell, "Stress-controlled elastic granular shear flows," *J. Fluid Mech.* **539**, 273 (2005).

[Cro96] J.C. Crocker, and D.G. Grier, "Methods of digital video microscopy for colloidal studies", *J. Colloid Interf. Sci.* **179**, 298 (1996).

[Cuc99] T. Cuccovillo and M.R. Coop, "On the mechanics of structured sands," *Géotechnique* **49**, 741 (1999).

[DaC05] F. Da Cruz, S. Emam, M. Prochnow, J.-N. Roux, and F. Chevoir, "Rheophysics of dense granular materials: Discrete simulation of plane shear flows," *Phys. Rev. E* **72**, 21309 (2005).

- [Est11] N. Estrada, E. Azéma, F. Radjaï, and A. Taboada, "Identification of rolling resistance as a shape parameter in sheared granular media," *Phys. Rev. E* **84**, 11306 (2011).
- [Fen04] D. Fenistein, J.W. van de Meent, and M. van Hecke, "Universal and wide shear zones in granular bulk flow," *Phys. Rev. Lett.* **92**, 094301 (2004).
- [Gou07] C.M. Gourlay, and A.K. Dahle, "Dilatant shear bands in solidifying metals," *Nature* **445**, 70 (2007).
- [Guo12] P. Guo, "Critical length of force chains and shear band thickness in dense granular materials," *Acta Geotech.* **7**, 41 (2012).
- [Han16] L. Handl, L. Torbahn, A. Spettl, H. Zetzener, V. Schmidt, and A. Kwade, "Microstructural changes, particle tracking and shear localization of fine glass powders," *Proceedings of the International Congress on Particle Technology, Nürnberg, 2016*, paper-ID 2.29.
- [Han17] L. Handl, L. Torbahn, A. Spettl, V. Schmidt, and A. Kwade, "Structural analysis and tracking of micron-sized glass particles during shear deformation: A study based on time-resolved tomographic data," *Adv. Powder Technol.* **28**, 1920 (2017).
- [Lud08] S. Luding, "Cohesive, frictional powders: Contact models for tension," *Granular Matter* **10**, 235 (2008).
- [MiD04] GDR MiDi, "On Dense Granular Flows," *Eur. Phys. J. E* **14**, 341 (2004).
- [Moo13] R. Moosavi, M.R. Shaebani, M. Maleki, J. Török, D.E. Wolf, and W. Losert, "Coexistence and transition between shear zones in slow granular flows," *Phys. Rev. Lett.* **111**, 148301 (2013).
- [Nem01] S. Nemat-Nasser, and N. Okada, "Radiographic and microscopic observation of shear bands in granular materials," *Géotechnique* **51**, 753 (2001).
- [Ons31a] L. Onsager, "Reciprocal relations in irreversible processes. I.," *Phys. Rev.* **37**, 405 (1931).
- [Ons31b] L. Onsager, "Reciprocal relations in irreversible processes. II.," *Phys. Rev.* **38**, 2265 (1931).
- [Rie16] A. Ries, L. Brendel, and D.E. Wolf, "Shear rate diffusion and constitutive relations during transients in simple shear," *Comput. Part. Mech.* **3**, 303 (2016).
- [Rie17] A. Ries, L. Brendel, and D.E. Wolf, "The cooperativity length in simple shear of dry granular media," *Comput. Part. Mech.* **4**, 379 (2017).
- [Rog08] P.G. Rognon, J.-N. Roux, M. Naaim, and F. Chevoir, "Dense flows of cohesive granular materials," *J. Fluid Mech.* **596**, 21 (2008).
- [Rog15] P.G. Rognon, T. Miller, B. Metzger, and I. Einav, "Long-range wall perturbations in dense granular flows," *J. Fluid Mech.* **764**, 171 (2015).

- [Rot04] L. Rothenburg and N.P. Kruyt, "Critical state and evolution of coordination number in simulated granular materials," *Int. J. Solids Struct.* **41**, 5763 (2004).
- [Sch03] J. Schwedes, "Review on testers for measuring flow properties of bulk solids," *Granul. Matter* **5**, 1 (2003).
- [Sch09] D. Schulze, *Pulver und Schüttgüter*, Springer Berlin Heidelberg, 2009.
- [Sho12a] Z. Shojaaee, J.-N. Roux, F. Chevoir, and D.E. Wolf, "Shear flow of dense granular materials near smooth walls. I. Shear localization and constitutive laws in the boundary region," *Phys. Rev. E* **86**, 11301 (2012).
- [Sho12b] Z. Shojaaee, L. Brendel, J. Török, and D.E. Wolf, "Shear flow of dense granular materials near smooth walls. II. Block formation and suppression of slip by rolling friction," *Phys. Rev. E* **86**, 11302 (2012).
- [Sod03] T. Soddemann, B. Dünweg, and K. Kremer, "Dissipative particle dynamics: A useful thermostat for equilibrium and nonequilibrium molecular dynamics simulations," *Phys. Rev. E* **68**, 046702 (2003).
- [Ste11] T. Stegmann, J. Török, L. Brendel, and D.E. Wolf, "Minimal dissipation theory and shear bands in biaxial tests," *Granular Matter* **13**, 565 (2011).
- [Str14a] S. Strege, A. Weuster, H. Zetzener, L. Brendel, A. Kwade, and D.E. Wolf, "Approach to structural anisotropy in compacted cohesive powder," *Granular Matter* **16**, 401 (2014).
- [Str14b] S. Strege, "Röntgenmikrotomographische Analyse der Verdichtung und Scherung feiner und kohäsiver Pulver", Ph.D. Thesis, TU Braunschweig, 2014, ISBN 978-3868446647.
- [Tho17] C. Thornton, S.J. Cummins, and P.W. Cleary, "On elastic-plastic normal contact force models, with and without adhesion," *Powder Technol.* **315**, 339 (2017).
- [Tho98] C. Thornton and Z.M. Ning, "A theoretical model for the stick/bounce behaviour of adhesive, elastic-plastic spheres," *Powder Technol.* **99**, 154 (1998).
- [Tig12] B.P. Tighe, "Critical viscoelastic response in jammed solids," arXiv:1205.2960 (2012).
- [Tom97] J. Tomas, "The consolidation of particulate solids - Microprocesses of caking and kinetic models," *Chemie Ing. Tech.* **69**, 455 (1997).
- [Tom07] J. Tomas, "Adhesion of ultrafine particles - A micromechanical approach," *Chem. Eng. Sci.* **62**, 1997 (2007).
- [Tor17] L. Torbahn, A. Weuster, L. Handl, V. Schmidt, A. Kwade, and D.E. Wolf, "Mesostructural investigation of micron-sized glass particles during shear deformation - An experimental approach vs. DEM simulation," *EPJ Web of Conferences* **140**, 03027 (2017).
- [Ung04] T. Unger, J. Török, J. Kertész, and D.E. Wolf, "Shear band formation in granular media as a variational problem," *Phys. Rev. Lett.* **92**, 214301 (2004).

[Wen13] J. Wenzl, R. Seto, M. Roth, H.-J. Butt, and G.K. Auernhammer, "Measurement of rotation of individual spherical particles in cohesive granulates," *Granular Matter* **15**, 391 (2013).

[Weu13] A. Weuster, L. Brendel, and D.E. Wolf, "Simulation of sheared, caking powder," in *AIP Conference Proceedings* **1542**, 515 (2013).

[Weu15] A. Weuster, S. Strege, L. Brendel, H. Zetzener, D.E. Wolf, and A. Kwade, "Shear flow of cohesive powders with contact crystallization: Experiment, model and calibration," *Granular Matter* **17**, 271 (2015).

[Weu17] A. Weuster, "Planare Scherung kohäsiver und zeitverfestigender granularer Materie mit der Diskrete-Elemente-Methode," Ph.D. thesis, Universität Duisburg-Essen, 2017.

[https://duepublico2.uni-due.de/receive/duepublico\\_mods\\_00044560](https://duepublico2.uni-due.de/receive/duepublico_mods_00044560)

[Woo90] D.M. Wood, *Soil Behaviour and Critical State Soil Mechanics*, Cambridge University Press, 1990.